
Look, Radiate, and Learn: Self-supervised Localisation via Radio-Visual Correspondence

Mo Alloulah
Bell Labs

Max Arnold
Bell Labs

Abstract

Next generation cellular networks will implement radio sensing functions alongside customary communications, thereby enabling unprecedented worldwide sensing coverage outdoors. Deep learning has revolutionised computer vision but has had limited application to radio perception tasks, in part due to lack of systematic datasets and benchmarks dedicated to the study of the performance and promise of radio sensing. To address this gap, we present MaxRay: a synthetic radio-visual dataset and benchmark that facilitate precise target localisation in radio. We further propose to learn to localise targets in radio without supervision by extracting self-coordinates from radio-visual correspondence. We use such self-supervised coordinates to train a radio localiser network. We characterise our performance against a number of state-of-the-art baselines. Our results indicate that accurate radio target localisation can be automatically learned from paired radio-visual data without labels, which is highly relevant to empirical data. This opens the door for vast data scalability and may prove key to realising the promise of robust radio sensing atop a unified perception-communication cellular infrastructure. Dataset will be hosted on IEEE DataPort.

1 Introduction

Sixth-generation (6G) wireless networks are being designed from the ground up to support sensing at the physical layer [1]. Such a brand new capability in 6G networks marks a departure from communication-only functions, and aims to supply applications with sensing primitives atop a unified communication-perception infrastructure. Concretely, dense cellular deployments in urban settings (e.g., per lamppost) would allow for unprecedented radio coverage, enabling a multitude of challenging perception tasks. Examples include around-the-corner obstacle detection in support of autonomous driving and pedestrian and drone localisation, to name a few [2].

Training perception models for radio signals is a key challenge for network infrastructure vendors. Unlike vision and audio, radio signals are hard to label manually because they are not human interpretable. Typically, sparse radio signals have been paired with a groundtruth vision modality for reliable semantic and qualitative filtration via a cross-modal annotation flow [3–6]. Recently, this radio-visual pairing has been shown to work in a self-supervised fashion [7], building on a wave of progress in vision self-supervised learning (SSL) [8–19].

Computer vision has traditionally benefited from synthetic datasets for: (a) content augmentation for enhanced generalisability [20, 21], or (b) closing the learning loop on out-of-distribution failure modes [22], e.g., in the context of autonomous driving [23]. Extrapolating from vision, it is also likely that synthetic data will play an important role towards realising robust radio sensing. However, radio perception tasks have yet to benefit from such publicly-available datasets.

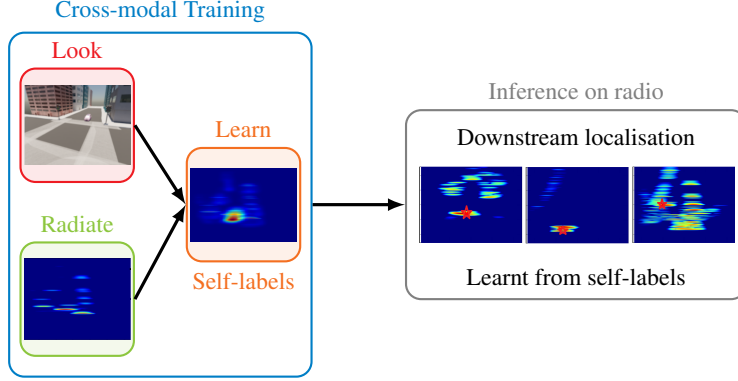


Figure 1: We train a radio localisation network by using commonalities with vision to drive spatial attention. Without laborious manual annotations, we learn to suppress clutter and localise targets in radio heatmaps.

In this work we aim to support next-gen 6G perception tasks, while championing a self-supervised radio-visual learning approach. Concretely, Fig. 1 captures the crux of our new machine learning proposition for radio sensing. We demonstrate how to automatically extract radio self-labels through cross-modal learning with vision. Such self-labels are then used to train a downstream localiser network. We show that our self-supervised localiser network enhances estimation in the radio domain compared to state-of-the-art.

To this end, we contribute two new radio-visual artefacts.

- A synthetic dataset: We curate and synthesise radio-visual data for a new learning task designed for target detection and localisation in radio.
- A cross-modal SSL algorithm: We formulate a contrastive radio-visual objective for label-free radio localisation.

We discuss our dataset and algorithmic findings to galvanise machine learners’ interest in radio-visual learning research. We hope to both facilitate and inform future research on this new cross-modal learning paradigm.

2 Related Work

Self-supervised learning. Self-supervised learning (SSL) in its two strands (contrastive and non-contrastive) is the state-of-the-art learning paradigm for visual representations [8–11]. SSL models have progressively matched and then exceeded the performance of their fully-supervised counterparts [12–15, 24, 25, 16–18], culminating recently in strong performance on uncurated billion-scale data [19]. Vision SSL relies on augmentation for semantic invariance. Differently, we deal with a new radio-visual SSL problem that relies on cross-modal correspondence [26, 27] as opposed to augmentation. Further, our work addresses SSL object detection and localisation using spatial backbone models [28, 29] rather than the prevalent object classification in vision using 1-D backbones.

Self-supervised multi-modal object detection. A related body of work leverages multiple modalities for representation learning, particularly between audio and vision [30, 26, 31–35, 27, 36]. Other works, also audio-visual, deal with knowledge distillation from one modality to another [37, 38]. SSL audio-visual object detectors are well researched and rely on feature attention between 1-D audio and 2-D vision [35, 29]. Differently in radio-visual, our attention (a) is complicated by a sparse radio modality which could impact the dimensional stability of cross-modal contrastive learning [39], and (b) involves a fundamentally larger feature search space between 2-D radio and 2-D vision.

Self-supervised saliency localisation. Recent works have extended visual saliency localisation [40, 41] for self-supervised systems [42]. Specifically, [43] expands class activation map (CAM) to work within an SSL network to markedly improve visual contrastive learning and mitigate against augmentation bias. While notable for vision SSL, radio-visual SSL does not suffer from the

augmentation-induced geometric perturbations during training (e.g., random crop and rotation) which make accurate object localisation trickier in vision SSL.

Radio learning. Recent works train radio models on vision-supplied labels for indoor human sensing, e.g., [4–6]. SSL has also been recently applied to radio-only learning systems. [44] proposes an SSL super-resolution method that improves the angular resolution of radar antenna arrays. [45] uses radar during training as a weak supervision signal, as well as an extra input to enhance depth estimation at inference time. [6] tackles the problem of radio-only SSL for human sensing. Our work is different from the above prior art in that it neither relies on explicit supervision from vision, nor it is single-modal for radio-only learning. A recent work proposes radio-visual SSL for object classification within a distillation framework [7]. This differs from our work which (a) deals with representation learning from scratch for both radio and vision and (b) is aimed at SSL object detection and localisation using an underlying spatial backbone as opposed to standard classification.

3 Dataset

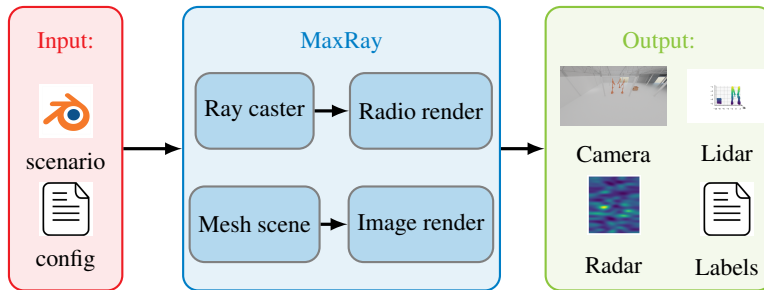


Figure 2: Block diagram of MaxRay.

Our radio-visual dataset is created using MaxRay [46]—a ray tracing tool for accurate radio propagation simulations. MaxRay also incorporates the open-source Blender engine for creating photo-realistic environments [47]. As such, we can model arbitrarily complex environments and synthesise paired responses in the vision and radio domains.

Fig. 2 depicts the tool block diagram. A Blender scenario and a configuration file (containing radio parameters such as carrier frequency and bandwidth) are inputted to MaxRay. MaxRay uses Python APIs to render responses for a variety of imaging sensors (e.g., camera, Lidar, depth images) along with their labels. The rendering and label quality allow us to train an off-the-shelf Yolo v5 models [48] from scratch. The core of MaxRay leverages the ray casting capability of Blender to simulate complex radio phenomena (e.g., scattering and reflection) and calculate their propagation losses. These propagation losses are then used to create channel state information (CSI), which is in turn converted to radar heatmaps according to an orthogonal frequency-division multiplexing (OFDM) signalling architecture. Note that when generating scenarios, objects are randomised and manipulated in Blender via Python APIs directly.

Table 1: Radio parameters used for data synthesis.

| RX array dimensions | Bandwidth | Carrier | Range-Azimuth Bins |
|---------------------|-----------|---------|--------------------|
| 16×16 | 800MHz | 28GHz | 480×640 |

The current version of the dataset supports the sensor configurations listed in Tab. 2. All available sensors are paired and synchronised per data point, facilitating cross-modal learning. Tab. 1 lists the radio configurations used in dataset, which comply with current 5G Advanced specifications [49]. Further, the dataset has sequences of 15 data points that allow for time series modelling.

The full version of the dataset has 3 scenarios: a parking lot, a suburban street, and a street canyon. Fig. 3 depicts one example per scenario. In parking lot, one car is driven from left to right or right to left. In suburban, one car drives along the house towards the camera or away from it. The same holds for the street canyon scenario. Note how radio heatmaps have different ranges, as well as different

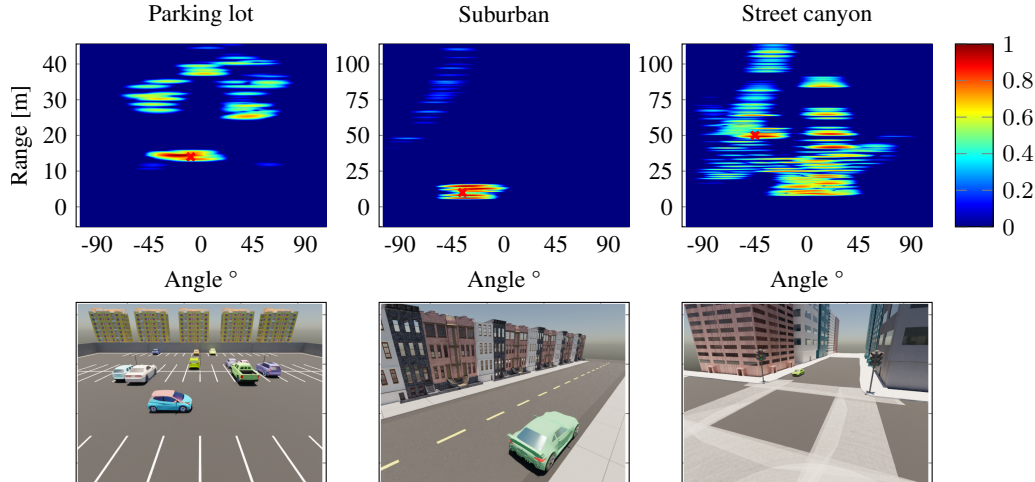


Figure 3: Example radio-visual radio-image pairs of three different scenarios: parking lot (left), suburban (middle), and street canyon (right)

Table 2: Paired entries in MaxRay. AoA: angle-of-arrival, AoD: angle-of-departure

| Entry | Data type | Label |
|--------|-----------|--|
| Camera | Image | bounding box + class |
| Lidar | Tensor | per point material + class |
| Depth | Image | bounding box + class |
| Radar | Image | bounding box (center) + reflectors + class |
| CSI | Tensor | reflectors + paths AoA/AoD |

amount of spurious clutter. For instance, parking lot has dynamic background clutter arising from changes in the location and pose of stationary cars across data points. Groundtruth information is supplied in the form of bounding boxes for vision and target coordinates for radar. In the terms of data diversity, there are 50 different cars, background and foreground randomised throughout the dataset. There are also portions of data that model mixed weather scenarios such as rain, snow, fog, and dust.

Phase 1 of dataset release focuses on the parking lot scenario only. For the remainder of this paper, we use parking lot with radar and camera entries. Specifically, parking lot has 30,000 paired radio-visual data points, split into 24k training and 6k validation sets. An additional 10k set is withheld for testing. All our results are reported on the 6k validation set.

4 Methods

We aim to automatically localise a target of interest in radio by tapping into the common information radio and its paired vision capture about the physical world. In fact, barring propagation nuances, radio imaging can be thought of as a low-resolution form of vision—Sec. D in Appendix justifies this view using a 1st-order analytic analysis derived from first principles. As such, jointly embedding radio and vision becomes not only a convenience, but is also naturally grounded in physics. Therefore, we would hope that the joint embedding architecture would constitute a powerful representation for building a wide variety of radio-only or combined radio-visual perception tasks. Concretely, our approach in this paper is to: (1) learn cross-modal spatial features via radio-visual correspondence, (2) extract self-estimates of target coordinates (i.e., pseudo labels) via cross-modal attention between the spatial features, and (3) use the self-coordinates to train a radio-only target localiser network. Fig. 4 illustrates this three-step procedure. In what follows, we explain further (1), (2), and (3).

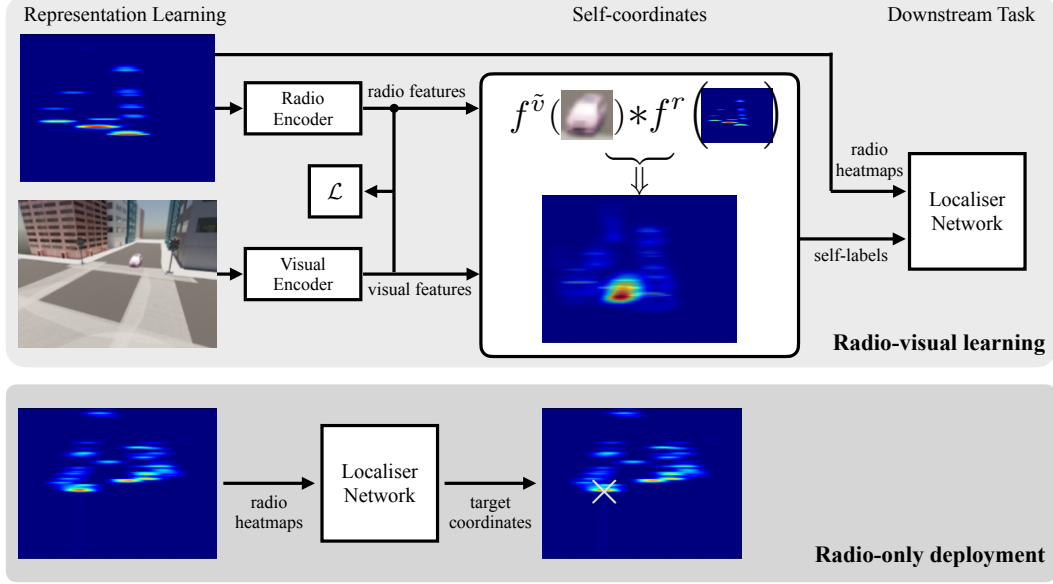


Figure 4: Radio target localisation via self-supervised radio-visual correspondence.

4.1 Representation learning

We employ a spatial flavour of contrastive learning we dub spatial contrastive learning (SCL) in order to self-localise targets in radio. SCL is inspired by earlier pioneering audio-visual learning works [27, 26], as well as more recent adaptations [35, 29, 50]. We begin by formalising SCL.

Spatial contrastive learning (SCL). Let (r, v) be a radio-visual data pair, where $r \in \mathbb{R}^{1 \times H \times W}$ is a radar heatmap and $v \in \mathbb{R}^{3 \times H \times W}$ is a corresponding RGB image. Encode, respectively, radio and vision by two backbone neural networks f_{θ^r} and f_{θ^v} , assuming some weight parametrisation $\{\theta^r, \theta^v\}$. Each backbone network encodes per bin one C -dimensional feature vector within 2-dimensional spatial bins, i.e., $f_{\theta^r}(r), f_{\theta^v}(v) \in \mathbb{R}^{C \times h \times w}$. The spatial binning resolution $h \times w$ is generally coarser than the original image resolution $H \times W$. Denote by $f_n^r(r), f_n^v(v) \in \mathbb{R}^C$ radio and vision spatial encodings at bin $n \in \Omega = \{1, \dots, h\} \times \{1, \dots, w\}$. Construct a target mask $\gamma := [\gamma_{ij}] \in [0, 1]^{H \times W}$ such that $f_m^v(\gamma \odot v) \in \mathbb{R}^C$ is defined for $m \in \tilde{\Omega} = \{1, \dots, \tilde{h}\} \times \{1, \dots, \tilde{w}\}$ to retain encodings for the target of interest only in the RGB image (e.g., as delineated by a bounding box), where \odot is the element-wise product and $\tilde{\Omega} \subset \Omega$ is a subset of spatial locations. In practice, the target mask can either be (1) estimated using off-the-shelf vision object detectors such as Yolo [51, 48], or (2) obtained directly as groundtruth during data synthesis. The visual spatial encodings of the masked target $f_m^v(\gamma \odot v)$ can be correlated against the radio spatial encodings covering of the entire sensing scene $f_n^r(r)$ in order to produce an attention map

$$h_n(r, v) = \text{conv2d}(f_n^r(r), f_m^v(\gamma \odot v)), \quad n \in \Omega, m \in \tilde{\Omega} \quad (1)$$

with appropriate padding.

To measure best cross-modal regional agreement, the attention map is maximised over spatial bins

$$S(r, v) = \max_{n \in \Omega} h_n(r, v) \quad (2)$$

Spatial cross-modal contrastive losses can then be implemented in a batch \mathcal{B} for all radio-visual pairs $(r, v) \in \mathcal{B}$ according to

$$\mathcal{L}_a^{v \rightarrow r}(\mathcal{B}) = -\mathbb{E}_{\mathcal{B}} \log \frac{\exp(S(r, v)/\tau)}{\sum_{i \in \mathcal{B}} \exp(S(r, v_i)/\tau)}, \quad \mathcal{L}_a^{r \rightarrow v}(\mathcal{B}) = -\mathbb{E}_{\mathcal{B}} \log \frac{\exp(S(r, v)/\tau)}{\sum_{i \in \mathcal{B}} \exp(S(r_i, v)/\tau)} \quad (3)$$

where the one-sided loss $\mathcal{L}_a^{v \rightarrow r}$ tests for vision-to-radio correspondence, similarly $\mathcal{L}_a^{r \rightarrow v}$ tests for radio-to-vision, and τ is a temperature hyper-parameter. The bidirectional contrastive loss that

incentivises cross-modal spatial attention becomes

$$\mathcal{L}_{\text{SCL}} = (\mathcal{L}_a^{v \rightarrow r} + \mathcal{L}_a^{r \rightarrow v})/2 \quad (4)$$

4.2 Target self-estimation

Once the backbone networks are learned and their spatial features are stable, we can use cross-modal attention maximisation (cf., Eqs. 1 & 2) to self-generate target coordinate estimates. This self-labelling is inherently noisy, but remarkably powerful. Particularly, a downstream localiser network is able to smooth these self-estimates when trained over a sufficiently large number of data points—as determined by the mutual information with perfect coordinates [52].

Rescaling and calibration. Target coordinate estimates are obtained in the spatial feature grid $h \times w$. We rescale to bring back to original grid $H \times W$, and perform one-off calibration for systematic offsets on entire dataset.

4.3 Localiser network

We construct the dataset $(r, \hat{y}) \in \mathcal{D}_{\text{loc}}$ from tuples of radio heatmaps r and their target self-labels \hat{y} . The localiser network is trained to regress \hat{y} from r using a mean squared error (MSE) loss.

5 Benchmarks

5.1 Baselines

Radar target detection is a historic and thoroughly investigated topic as it pertains to many civil and military applications. The objective is to predict a target’s position and velocity. However, extracting wanted information (i.e., the target) from unwanted information (i.e., clutter) is a challenging task. Due to radio propagation phenomena, both could exhibit comparable statistical behaviour. We implement expert statistical techniques used by various industries in millions of products, and designate as our first strong standard baseline. Equally, a fully-supervised localiser network trained on groundtruth coordinates naturally forms our second deep learning-based baseline. In what follows, we describe in more detail these two approaches.

Statistical. Extracting information from a radio response representation is a multi-step procedure. First, radio targets in two different domains, range-angle and range-velocity, are binarised via a threshold technique (e.g., CFAR [53]) and then clustered (e.g., via DBSCAN [54]) to form one point cloud per target. Targets are then matched between the two different domains over the same and hopefully unique range. Point cloud centroids are used to track targets.

Considering such multi-step procedure, the following shortcomings come to mind. First, how to detect from the matched targets the wanted target (e.g., how to remove clutter). Second, some information is ignored (e.g., information from the shape of the point clouds) when assigning a target centroid. Third, setting the optimal thresholds, guard bands, training bands, number of points per cluster [53] is an exceedingly brittle exercise. It is our hope that end-to-end deep learning is able to address some of the aforementioned shortcomings.

Supervised. In radio sensing, the notion of supervised learning is intractable to implement under practical settings. This is because labelling radio heatmaps (e.g., object centre, type, bounding box) is infeasible as we cannot interpret the scene by manual inspection. However, we consider the supervised use case of training on synthetic data and deploying a finetuned model on empirical data.

Compared to computer vision, radio imaging is an immature sensing modality and there are no prescribed or de facto neural architectures to use for evaluation. We therefore use Microsoft’s AutoML tool NNI (Neural Network Intelligence) [55] to search for strong candidate architectures. Specifically, we searched for optimizers, loss functions, learning rates, momentum, neural architectures via resolution branching, and activation functions. The performance of the supervised baseline in Sec. 6 corroborates the quality of the search. Detailed description of the architectural search space is given in Sec. A.

5.2 Implementation details

The spatial backbone of the radio and vision encoders uses an architecture similar to VGG-M [28, 27], swapping max pooling for average pooling as recommended in [29].

For standard contrastive ablation in Sec. 6.2 (Contrastive Loss (CL) & Masked contrastive Loss (MCL)), we base our cross-modal contrastive learning on MoCo v2 and its public implementation [9]. We extend MoCo’s implementation with two queues for radio and vision similar to the audio-visual active sampling work in [56]. We have found that filtering the encoders with exponential moving average (EMA) when implementing radio-vision contrast has no tangible advantage, as detailed in Sec. C.

For estimating object bounding boxes for mask generation in vision, we rely on groundtruth from Blender for efficiency reasons as loading Yolo along with spatial backbones into GPU memory proved tricky. However, we did train a YoloV5 model [48] from scratch and optimised it for our synthetic radio-visual dataset, showing that it works in the same accuracy as the original one. Specifically, we reduced the number of classes supported by detection to considerably shrink the model size. We plan on augmenting a future version of the dataset with pseudo bounding boxes obtained from our version of YoloV5.

We train on 640×480 resolution for both RGB images and radio heatmaps. Both radio and vision branches output $128 \times 80 \times 60$ spatial features whose dimensionality is reduced using 2-layer MLP projectors to 64-D vectors in the case of CL & MCL. For CL & MCL, we use a MoCo v2 queue whose size equals to the batch size. For CL & MCL, the temperature hyper-parameter is 0.07, whereas for SCL it is 0.1. When implementing spatial attention, we pad bounding boxes by a margin of 5 pixels, and pad a target spatial response by a margin of 1 feature. For backbone training, we use the Adam optimiser [57] with a learning rate of 10^{-5} and no schedule. For all model variants, we train for 200 epochs with a batch size of 32. We use a batch size of 32 and train in a distributed fashion on 8 GeForce RTX 2080 Ti GPUs. We use two such GPUs throughout for backbone training, supervised training, and NNI search space. Backbone training takes around 16 hours per experiment. Both the localiser network trained on self-coordinates and supervised baseline use identical architecture and training as detailed in Tab. 5. Training the NNI model takes about 2 hours per model. The NNI search space took around 5 days.

6 Results

Having described our benchmarking setup in Sec. 5, we turn next to discussing results. All results are computed on 6k data points of validation set. We further conduct an ablation study of SCL against more common contrastive architectures in order to concretely understand the benefit of spatial contrast.

6.1 Localisation

We examine the overall performance of our SCL-based self-labelled localiser network and compare it against that fully supervised baseline and statistical baselines. The self-labelled network and supervised baseline share identical architecture and training configurations. We denote the statistical baseline by Constant-False-Alarm-Rate (CFAR). Tab. 3 summarises the performance in terms of 50th %ile and 90th %ile localisation errors. Not surprisingly, the fully-supervised network performs most favourably with around 30cm median error and under 1m at 90th %ile. SCL comes second with approx. 1.5m and 3.5m errors, respectively. This is remarkable given that SCL has automatically learned how to localise targets by simply observing paired radio-visual data. Statistical CFAR performs worst with roughly $1.8 \times$ SCL’s median error and $2.3 \times$ SCL’s 90th %ile error.

6.2 Spatial contrast versus projector contrast

SCL has appeared in multiple recent works that use 2-D backbone modelling [35, 29, 50]. However, the majority of SSL works dealing with image classification use 1-D feature vector backbones proceeded by projector heads where the actual contrastive loss is computed [8]. In this section, we investigate the performance of model variants with 2-D backbones similar to SCL; however, with contrastive learning implemented using a projector head that collapses the spatial encodings into a

Table 3: Performance of various methods: Supervised, SCL, and CFAR.

| Method | Perf. (error in m) | |
|------------|--------------------|-------------------|
| | 50th %ile | 90th %ile |
| Supervised | 0.289 ± 0.017 | 0.922 ± 0.042 |
| SCL | 1.571 ± 0.050 | 3.539 ± 0.062 |
| CFAR | 2.709 | 8.062 |

1-D feature vector. Specifically, we implement two methods: (1) vanilla contrastive learning (CL), and (2) masked contrastive learning (MCL) whereby the visual image is first multiplied by a mask as to only retain the target of interest before performing radio-visual CL. For formal definitions of CL & MCL in the radio-visual setting, the reader is directed to Sec. B. Once CL & MCL are trained, we derive self-labels in similar fashion to SCL using Eqs. 1 & 2 and then train respective localiser networks. We ask: *What role does the spatial attention loss play during learning and could it be absorbed by the projector head?*

Table 4: Backbone training configurations. CL: contrastive, MCL: masked contrastive, SCL: spatial contrastive

| Configuration | Perf. (error in m) | |
|---------------|--------------------|--------------------|
| | 50th %ile | 90th %ile |
| SCL | 1.571 ± 0.050 | 3.539 ± 0.062 |
| MCL | 0.942 ± 0.016 | 4.681 ± 0.158 |
| CL | 3.111 ± 0.358 | 17.498 ± 0.317 |

Tab. 4 analyses the performance of the three backbone configurations. We note that vanilla CL performs poorly with 3.1m and 17.5m errors, respectively at the 50th and 90th %iles. We attribute the high localisation errors to the lack of target sensitivity of CL during training. MCL, on the other hand, is trained to attend to targets through masking and exhibits a 50th %ile error of 0.94m, interestingly 1/3rd better than SCL. A closer look at MCL’s 90th %ile error at 4.6m reveals that it is also around $1.3\times$ “lazier” than SCL at tracking higher %ile targets. We conjecture that SCL is spatially more sound as it is able to better deal with targets that are likely to correspond to harder cases. Finally, we note that SCL is computationally much more efficient than CL and MCL since it does not rely on the 2-layer MLP projector. Projector heads tend to be rather large in parameter size.

Fig 5 depicts the full error cumulative density functions (CDFs) of all methods: CFAR, supervised, SCL, and MCL.

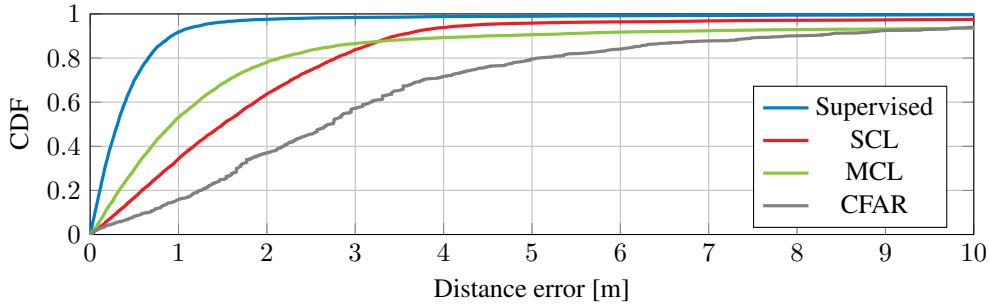


Figure 5: Localisation error CDFs of methods: CFAR, supervised, SCL, and MCL

6.3 Label density analysis

Using our 24k training set, we sweep the amount of labels and self-labels used to train the localiser networks of supervised, SCL, and MCL. Then we evaluate on the validation set to gauge the localisation performance sensitivity to the amount of available training (self-)labels. We cover the training points in logarithmic steps.

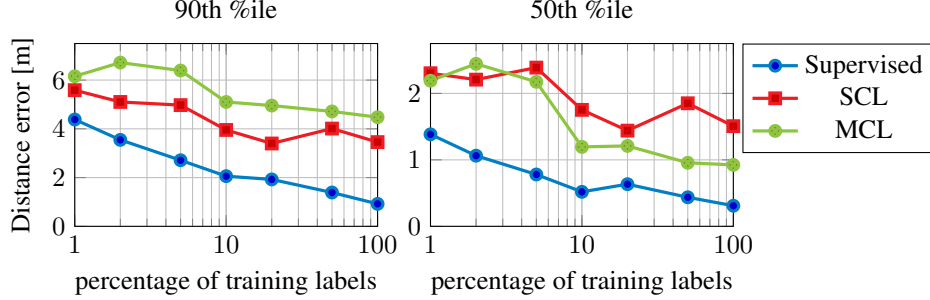


Figure 6: Effect of number of training labels on localisation performance for supervised, SCL, and MCL.

With the noisy labels of SCL and MCL, it can be shown that the localiser networks learn to compensate for such noise by using sufficiently large number of data points [52]. The number of required data points is a function of the mutual information between noisy target coordinates and perfect coordinates [52]. Fig. 6 examines this effect for supervised as a reference baseline, and SCL and MCL. We observe that SCL has a better label density tolerance than MCL w.r.t. the 90th %ile performance. The opposite holds true at the 50th %ile performance, i.e. MCL is better than SCL. This finding mirrors the localisation error analysis of Fig. 5 and is in line with our earlier conjecture; SCL seems to cope better with corner cases than MCL, while MCL seems to be a better self-localiser of the bulk of the distribution of the validation set.

7 Conclusion

In this paper, we present a new radio-visual learning task for emerging 6G cellular networks. The task tackles the problem of accurate target localisation in radio, employing a novel learning paradigm that works by simply ingesting large quantities of paired radio-visual data. This is in stark opposition to supervised and/or classic statistical methods whose success hinges on laborious labelling and/or modelling of empirical measurements, which are expensive to scale. Our novel target localisation paradigm is made possible by a new dataset and benchmark intended to foster future research on radio sensing for next generation cellular systems.

Limitations. We note that radio sensing capabilities are fundamentally set by the choice of configurations in Tab. 1. We have opted to base this somewhat conservative choice on 5G Advanced specifications [49] in order to inform cellular stakeholder discussions. We would, however, note that much improved radio sensing performance can be attained through increased bandwidth and/or denser antenna arrays, such as in Terahertz or even higher Millimeter-wave bands [58, 59]. We would refine our dataset and results in light of future consensus on 6G sensing specifications.

Broader impact. Our work has a broader societal impact in that it has the potential to alleviate some of risks associated with the surveillance economy. Specifically, once trained and deployed, our radio sensing system offers a scalable alternative to pervasive vision surveillance that is inherently privacy-preserving—both at the individual and societal levels—while achieving many of the sought-after safety and security benefits.

8 Acknowledgments

We thank Dmitry Chizhik for his analytic modelling of the relationship between radio imaging and vision in Sec. D. We would like to thank Howard Huang, Akash Singh and Prof. Mani Srivastava for their helpful discussions.

References

- [1] Thorsten Wild, Volker Braun, and Harish Viswanathan. Joint design of communication and sensing for beyond 5G and 6G systems. *IEEE Access*, 9:30845–30857, 2021.
- [2] A. Bourdoux, et. al. 6G White Paper on Localization and Sensing, 2020.
- [3] Yizhou Wang, Zhongyu Jiang, Yudong Li, Jenq-Neng Hwang, Guanbin Xing, and Hui Liu. Rodnet: A real-time radar object detection network cross-supervised by camera-radar fused object 3D localization. *IEEE Journal of Selected Topics in Signal Processing*, 15(4):954–967, 2021.
- [4] Mingmin Zhao, Tianhong Li, Mohammad Abu Alsheikh, Yonglong Tian, Hang Zhao, Antonio Torralba, and Dina Katabi. Through-wall human pose estimation using radio signals. In *Proceedings of the IEEE Conference on Computer Vision and Pattern Recognition*, pages 7356–7365, 2018.
- [5] Tianhong Li, Lijie Fan, Mingmin Zhao, Yingcheng Liu, and Dina Katabi. Making the invisible visible: Action recognition through walls and occlusions. In *Proceedings of the IEEE/CVF International Conference on Computer Vision*, pages 872–881, 2019.
- [6] Lijie Fan, Tianhong Li, Rongyao Fang, Rumen Hristov, Yuan Yuan, and Dina Katabi. Learning longterm representations for person re-identification using radio signals. In *Proceedings of the IEEE/CVF Conference on Computer Vision and Pattern Recognition*, pages 10699–10709, 2020.
- [7] Mohammed Alloulah, Akash Deep Singh, and Maximilian Arnold. Self-supervised radio-visual representation learning for 6G sensing. *arXiv preprint arXiv:2111.02887*, 2021.
- [8] Ting Chen, Simon Kornblith, Mohammad Norouzi, and Geoffrey Hinton. A simple framework for contrastive learning of visual representations. In *International conference on machine learning*, pages 1597–1607. PMLR, 2020.
- [9] Kaiming He, Haoqi Fan, Yuxin Wu, Saining Xie, and Ross Girshick. Momentum contrast for unsupervised visual representation learning. In *Proceedings of the IEEE/CVF Conference on Computer Vision and Pattern Recognition*, pages 9729–9738, 2020.
- [10] Jean-Bastien Grill, Florian Strub, Florent Altché, Corentin Tallec, Pierre Richemond, Elena Buchatskaya, Carl Doersch, Bernardo Avila Pires, Zhaohan Guo, Mohammad Gheshlaghi Azar, et al. Bootstrap your own latent-a new approach to self-supervised learning. *Advances in Neural Information Processing Systems*, 33:21271–21284, 2020.
- [11] Jure Zbontar, Li Jing, Ishan Misra, Yann LeCun, and Stéphane Deny. Barlow twins: Self-supervised learning via redundancy reduction. In *International Conference on Machine Learning*, pages 12310–12320. PMLR, 2021.
- [12] Mehdi Noroozi and Paolo Favaro. Unsupervised learning of visual representations by solving jigsaw puzzles. In *European conference on computer vision*, pages 69–84. Springer, 2016.
- [13] Richard Zhang, Phillip Isola, and Alexei A Efros. Colorful image colorization. In *European conference on computer vision*, pages 649–666. Springer, 2016.
- [14] Spyros Gidaris, Praveer Singh, and Nikos Komodakis. Unsupervised representation learning by predicting image rotations. *arXiv preprint arXiv:1803.07728*, 2018.
- [15] Aaron van den Oord, Yazhe Li, and Oriol Vinyals. Representation learning with contrastive predictive coding. *arXiv preprint arXiv:1807.03748*, 2018.
- [16] Mathilde Caron, Ishan Misra, Julien Mairal, Priya Goyal, Piotr Bojanowski, and Armand Joulin. Unsupervised learning of visual features by contrasting cluster assignments. *arXiv preprint arXiv:2006.09882*, 2020.
- [17] Olivier Henaff. Data-efficient image recognition with contrastive predictive coding. In *International Conference on Machine Learning*, pages 4182–4192. PMLR, 2020.
- [18] Adrien Bardes, Jean Ponce, and Yann LeCun. Vicreg: Variance-invariance-covariance regularization for self-supervised learning. *arXiv preprint arXiv:2105.04906*, 2021.
- [19] Priya Goyal, Quentin Duval, Isaac Seessel, Mathilde Caron, Mannat Singh, Ishan Misra, Levent Sagun, Armand Joulin, and Piotr Bojanowski. Vision models are more robust and fair when pretrained on uncured images without supervision. *arXiv preprint arXiv:2202.08360*, 2022.

- [20] Philipp Krähenbühl. Free supervision from video games. In *Proceedings of the IEEE Conference on Computer Vision and Pattern Recognition*, pages 2955–2964, 2018.
- [21] Yue Yao, Liang Zheng, Xiaodong Yang, Milind Naphade, and Tom Gedeon. Simulating content consistent vehicle datasets with attribute descent. In *European Conference on Computer Vision*, pages 775–791. Springer, 2020.
- [22] Sebastian Risi and Julian Togelius. Increasing generality in machine learning through procedural content generation. *Nature Machine Intelligence*, 2(8):428–436, 2020.
- [23] Tesla AI day. URL <https://www.youtube.com/watch?v=j0z4FweCy4M&t=5715s>.
- [24] R Devon Hjelm, Alex Fedorov, Samuel Lavoie-Marchildon, Karan Grewal, Phil Bachman, Adam Trischler, and Yoshua Bengio. Learning deep representations by mutual information estimation and maximization. *arXiv preprint arXiv:1808.06670*, 2018.
- [25] Philip Bachman, R Devon Hjelm, and William Buchwalter. Learning representations by maximizing mutual information across views. *Advances in neural information processing systems*, 32, 2019.
- [26] Relja Arandjelovic and Andrew Zisserman. Look, listen and learn. In *Proceedings of the IEEE International Conference on Computer Vision*, pages 609–617, 2017.
- [27] Relja Arandjelovic and Andrew Zisserman. Objects that sound. In *Proceedings of the European conference on computer vision*, pages 435–451, 2018.
- [28] Ken Chatfield, Karen Simonyan, Andrea Vedaldi, and Andrew Zisserman. Return of the devil in the details: Delving deep into convolutional nets. *arXiv preprint arXiv:1405.3531*, 2014.
- [29] Triantafyllos Afouras, Yuki M Asano, Francois Fagan, Andrea Vedaldi, and Florian Metze. Self-supervised object detection from audio-visual correspondence. *arXiv preprint arXiv:2104.06401*, 2021.
- [30] Humam Alwassel, Dhruv Mahajan, Bruno Korbar, Lorenzo Torresani, Bernard Ghanem, and Du Tran. Self-supervised learning by cross-modal audio-video clustering. *Advances in Neural Information Processing Systems*, 33:9758–9770, 2020.
- [31] Yuki Markus Asano, Christian Rupprecht, and Andrea Vedaldi. Self-labelling via simultaneous clustering and representation learning. *arXiv preprint arXiv:1911.05371*, 2019.
- [32] Yusuf Aytar, Carl Vondrick, and Antonio Torralba. Soundnet: Learning sound representations from unlabeled video. *Advances in neural information processing systems*, 29, 2016.
- [33] Pedro Morgado, Yi Li, and Nuno Nvasconcelos. Learning representations from audio-visual spatial alignment. *Advances in Neural Information Processing Systems*, 33:4733–4744, 2020.
- [34] Andrew Owens, Jiajun Wu, Josh H McDermott, William T Freeman, and Antonio Torralba. Ambient sound provides supervision for visual learning. In *European conference on computer vision*, pages 801–816. Springer, 2016.
- [35] Triantafyllos Afouras, Andrew Owens, Joon Son Chung, and Andrew Zisserman. Self-supervised learning of audio-visual objects from video. In *Computer Vision–ECCV 2020: 16th European Conference, Glasgow, UK, August 23–28, 2020, Proceedings, Part XVIII* 16, pages 208–224. Springer, 2020.
- [36] Honglie Chen, Weidi Xie, Triantafyllos Afouras, Arsha Nagrani, Andrea Vedaldi, and Andrew Zisserman. Localizing visual sounds the hard way. In *Proceedings of the IEEE/CVF Conference on Computer Vision and Pattern Recognition*, pages 16867–16876, 2021.
- [37] Chuang Gan, Hang Zhao, Peihao Chen, David Cox, and Antonio Torralba. Self-supervised moving vehicle tracking with stereo sound. In *Proceedings of the IEEE/CVF International Conference on Computer Vision*, pages 7053–7062, 2019.
- [38] Triantafyllos Afouras, Joon Son Chung, and Andrew Zisserman. Asr is all you need: Cross-modal distillation for lip reading. In *ICASSP 2020-2020 IEEE International Conference on Acoustics, Speech and Signal Processing (ICASSP)*, pages 2143–2147. IEEE, 2020.
- [39] Li Jing, Pascal Vincent, Yann LeCun, and Yuandong Tian. Understanding dimensional collapse in contrastive self-supervised learning. *arXiv preprint arXiv:2110.09348*, 2021.
- [40] Bolei Zhou, Aditya Khosla, Agata Lapedriza, Aude Oliva, and Antonio Torralba. Learning deep features for discriminative localization. In *Proceedings of the IEEE conference on computer vision and pattern recognition*, pages 2921–2929, 2016.

- [41] Ramprasaath R Selvaraju, Michael Cogswell, Abhishek Das, Ramakrishna Vedantam, Devi Parikh, and Dhruv Batra. Grad-cam: Visual explanations from deep networks via gradient-based localization. In *Proceedings of the IEEE international conference on computer vision*, pages 618–626, 2017.
- [42] Kyungjune Baek, Minhyun Lee, and Hyunjung Shim. Psynet: Self-supervised approach to object localization using point symmetric transformation. In *Proceedings of the AAAI Conference on Artificial Intelligence*, volume 34, pages 10451–10459, 2020.
- [43] Sangwoo Mo, Hyunwoo Kang, Kihyuk Sohn, Chun-Liang Li, and Jinwoo Shin. Object-aware contrastive learning for debiased scene representation. *Advances in Neural Information Processing Systems*, 34, 2021.
- [44] Itai Orr, Moshik Cohen, Harel Damari, Meir Halachmi, and Zeev Zalevsky. Coherent, super resolved radar beamforming using self-supervised learning. *arXiv preprint arXiv:2106.13085*, 2021.
- [45] Stefano Gasperini, Patrick Koch, Vinzenz Dallabetta, Nassir Navab, Benjamin Busam, and Federico Tombari. R4dyn: Exploring radar for self-supervised monocular depth estimation of dynamic scenes. *arXiv preprint arXiv:2108.04814*, 2021.
- [46] M Arnold, M Bauhofer, S Mandelli, M Henninger, F Schaich, T Wild, and S ten Brink. Maxray: A raytracing-based integrated sensing and communication framework. In *2022 2nd IEEE International Symposium on Joint Communications & Sensing (JC&S)*, pages 1–7. IEEE, 2022.
- [47] Blender Online Community. Free and open 3D creation software. URL <https://www.blender.org>.
- [48] Glenn Jocher et. al. ultralytics/yolov5: v6.0 - YOLOv5n 'Nano' models, Roboflow integration, TensorFlow export, OpenCV DNN support, October 2021. URL <https://doi.org/10.5281/zenodo.5563715>.
- [49] Younsun Kim, Youngbum Kim, Jinyoung Oh, Hyoungju Ji, Jeongho Yeo, Seunghoon Choi, Hyunseok Ryu, Hoondong Noh, Taehyoung Kim, Feifei Sun, et al. New radio (NR) and its evolution toward 5G-advanced. *IEEE Wireless Communications*, 26(3):2–7, 2019.
- [50] Rhyddian Windsor, Amir Jamaludin, Timor Kadir, and Andrew Zisserman. Self-supervised multi-modal alignment for whole body medical imaging. In *International Conference on Medical Image Computing and Computer-Assisted Intervention*, pages 90–101. Springer, 2021.
- [51] Joseph Redmon, Santosh Divvala, Ross Girshick, and Ali Farhadi. You only look once: Unified, real-time object detection. In *Proceedings of the IEEE conference on computer vision and pattern recognition*, pages 779–788, 2016.
- [52] Melody Guan, Varun Gulshan, Andrew Dai, and Geoffrey Hinton. Who said what: Modeling individual labelers improves classification. In *Proceedings of the AAAI Conference on Artificial Intelligence*, volume 32, 2018.
- [53] Hermann Rohling. Radar CFAR thresholding in clutter and multiple target situations. *IEEE transactions on aerospace and electronic systems*, (4):608–621, 1983.
- [54] Martin Ester, Hans-Peter Kriegel, Jörg Sander, Xiaowei Xu, et al. A density-based algorithm for discovering clusters in large spatial databases with noise. In *KDD*, volume 96, pages 226–231, 1996.
- [55] Microsoft. Neural Network Intelligence, 1 2021. URL <https://github.com/microsoft/nni>.
- [56] Shuang Ma, Zhaoyang Zeng, Daniel McDuff, and Yale Song. Active contrastive learning of audio-visual video representations. *arXiv preprint arXiv:2009.09805*, 2020.
- [57] Diederik P Kingma and Jimmy Ba. Adam: A method for stochastic optimization. *arXiv preprint arXiv:1412.6980*, 2014.
- [58] Mohamed Elkhoully, Jaeyeon Ha, Michael J Holyoak, David Hendry, Mustafa Sayginer, Ryan Enright, Ioannis Kimionis, Yves Baeyens, and Shahriar Shahramian. Fully integrated 2D scalable TX/RX chipset for D-band phased-array-on-glass modules. In *2022 IEEE International Solid-State Circuits Conference (ISSCC)*, volume 65, pages 76–78. IEEE, 2022.
- [59] Shahriar Shahramian, Michael J Holyoak, Amit Singh, and Yves Baeyens. A fully integrated 384-element, 16-tile, w -band phased array with self-alignment and self-test. *IEEE Journal of solid-state circuits*, 54(9): 2419–2434, 2019.
- [60] Yuandong Tian, Xinlei Chen, and Surya Ganguli. Understanding self-supervised learning dynamics without contrastive pairs. In *International Conference on Machine Learning*, pages 10268–10278. PMLR, 2021.
- [61] Timnit Gebru, Jamie Morgenstern, Briana Vecchione, Jennifer Wortman Vaughan, Hanna Wallach, Hal Daumé Iii, and Kate Crawford. Datasheets for datasets. *Communications of the ACM*, 64(12): 86–92, 2021.

A In-depth NNI explanation

Neural Network Intelligence (NNI) is an automatic-machine-learning (AutoML) tool allowing to chose different types of optimizing parameters. We show the different kind of optimization parameters we consider in the table 5.

Table 5: NNI optimization parameters

| Parameter | Explanation | Selection | Values | Best Net chosen |
|-----------|-----------------------------------|-----------|--|-----------------|
| lr | Learning rate | Choice | 0.0001, 0.001, 0.01 | 0.001 |
| momentum | Momentum for optimizer | Uniform | 0.8,...,1 | 0.948985588 |
| act_func | Activation function of conv layer | Choice | "ReLU", "LeakyReLU", "Sigmoid", "Tanh", "Softplus" | ReLU |
| optimizer | Optimizer type | Choice | "SGD", "Adam" | Adam |
| loss_func | Loss function for training only | Choice | "MSE", "L1" | MSE |
| c1_size | Convolutional kernels of Layer x | Choice | 4,8,16,32,64 | 8 |
| c2_size | Convolutional kernels of Layer x | Choice | 4,8,16,32,64 | 16 |
| c3_size | Convolutional kernels of Layer x | Choice | 4,8,16,32,64 | 8 |
| c4_size | Convolutional kernels of Layer x | Choice | 4,8,16,32,64 | 32 |
| k1_size | Kernel size of c1 layer | Choice | 2, 3, 4 | 4 |
| k2_size | Kernel size of c2 layer | Choice | 2, 3, 4 | 3 |
| k3_size | Kernel size of c3 layer | Choice | 2, 3, 4 | 2 |
| k4_size | Kernel size of c4 layer | Choice | 2, 3, 4 | 4 |
| s1_size | Stride of c1 layer | Choice | 1,2 | 2 |
| s2_size | Stride of c2 layer | Choice | 1,2 | 2 |
| s3_size | Stride of c3 layer | Choice | 1,2 | 2 |
| s4_size | Stride of c4 layer | Choice | 1,2 | 1 |
| lin1_size | Linear layer 1 | Choice | 128,256,512 | 128 |
| lin2_size | Linear layer 2 | Choice | 16, 32, 64, 128, 256 | 16 |
| lin3_size | Linear layer 3 | Choice | 16, 32, 64, 128, 256 | 64 |
| lin4_size | Linear layer 4 | Choice | 64, 182, 256 | 64 |

The best Neural Network (NN) parameters are shown in the right column in 5.

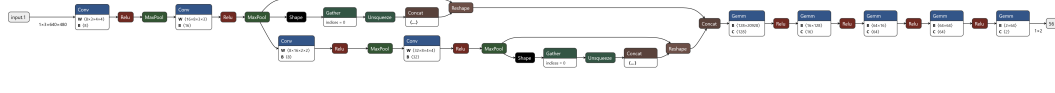


Figure 7: NN structure

Fig. 7 shows the effective structure of the supervised NN.

B Contrastive learning background & definitions

Contrastive learning (CL). Let (r, v) be a radio-visual data pair, where $r \in \mathbb{R}^{1 \times H \times W}$ is a radar heatmap and $v \in \mathbb{R}^{3 \times H \times W}$ is a corresponding RGB image. Encode, respectively, radio and vision by two neural networks f_{θ^r} and f_{θ^v} and their momentum-filtered versions $f_{\hat{\theta}^r}$ and $f_{\hat{\theta}^v}$, assuming some weight parametrisation $\{\theta^r, \theta^v\}$. Additionally, use projector heads g_{θ^r} and g_{θ^v} respectively, such that

$$q^r = g_{\theta^r}(f_{\theta^r}(r)), \quad k^v = g_{\theta^v}(f_{\hat{\theta}^v}(v)), \quad q^v = g_{\theta^v}(f_{\theta^v}(v)), \quad k^r = g_{\theta^r}(f_{\hat{\theta}^r}(r)) \quad (5)$$

where vectors $q^r, q^v, k^v, k^r \in \mathbb{R}^N$, superscripts r and v denote respectively radio and vision, and following MoCo's query q and key k notation [9]. With each r , use $K + 1$ samples of v of which one sample v^+ is a true match to r and K samples $\{v_i^-\}_{i=0}^{K-1}$ are false matches—vice versa with each v , $K + 1$ samples of r . The one-sided cross-modal contrastive losses that test for vision-to-radio and radio-to-vision correspondences are

$$\begin{aligned} \mathcal{L}_c^{v \rightarrow r}(q^r, k^{v^+}, \mathbf{k}^{v^-}) &= -\mathbb{E}_{r,v} \log \frac{\exp(q^r \cdot k^{v^+} / \tau)}{\exp(q^r \cdot k^{v^+} / \tau) + \sum_i \exp(q^r \cdot k_i^{v^-} / \tau)} \\ \mathcal{L}_c^{r \rightarrow v}(q^v, k^{r^+}, \mathbf{k}^{r^-}) &= -\mathbb{E}_{r,v} \log \frac{\exp(q^v \cdot k^{r^+} / \tau)}{\exp(q^v \cdot k^{r^+} / \tau) + \sum_i \exp(q^v \cdot k_i^{r^-} / \tau)} \end{aligned} \quad (6)$$

where \cdot is the dot product, $k^{x+/ -} = g_{\theta^x}(f_{\hat{\theta}^x}(x^{+/-}))$ are encodings that denote true and false corresponding signals $x \in [r, v]$, vector $\mathbf{k}^{x-} = \{k_i^{x-}\}_{i=0}^{K-1}$ holds K false encodings, and τ is a temperature hyper-parameter. Then the bidirectional cross-modal contrastive loss is

$$\mathcal{L}_{CL} = (\mathcal{L}_c^{v \rightarrow r} + \mathcal{L}_c^{r \rightarrow v}) / 2 \quad (7)$$

Masked contrastive learning (MCL). The projector heads g_{θ^r} and g_{θ^v} are MLPs that collapse the spatial encodings of the backbone networks f_{θ^r} and f_{θ^v} onto vector representations. Each backbone network encodes per bin one C -dimensional feature vector within 2-dimensional spatial bins, i.e., $f_{\theta^r}(r), f_{\theta^v}(v) \in \mathbb{R}^{C \times h \times w}$. The spatial binning resolution $h \times w$ is generally coarser than the original image resolution $H \times W$. Denote by $f_n^r(r), f_n^v(v) \in \mathbb{R}^C$ radio and vision spatial encodings at bin $n \in \Omega = \{1, \dots, h\} \times \{1, \dots, w\}$. Construct a target mask $\gamma := [\gamma_{ij}] \in [0, 1]^{H \times W}$ such that $f_m^v(\gamma \odot v) \in \mathbb{R}^C$ is defined for $m \in \tilde{\Omega} = \{1, \dots, \tilde{h}\} \times \{1, \dots, \tilde{w}\}$ to retain encodings for the target of interest only in the RGB image (e.g., as delineated by a bounding box), where \odot is the element-wise product and $\tilde{\Omega} \subset \Omega$ is a subset of spatial locations. In practice, the target mask can either be (1) estimated using off-the-shelf vision object detectors such as Yolo [51, 48], or (2) obtained directly as groundtruth during data synthesis. We can define contrastive losses to test for masked vision-to-radio and radio-to-masked vision correspondences, similar to Eq. 6. Using superscript \tilde{v} to denote masking in vision, then the bidirectional cross-modal contrastive loss with target masking becomes

$$\mathcal{L}_{\text{MCL}} = (\mathcal{L}_c^{\tilde{v} \rightarrow r} + \mathcal{L}_c^{r \rightarrow \tilde{v}})/2 \quad (8)$$

C Radio-visual subspace analysis

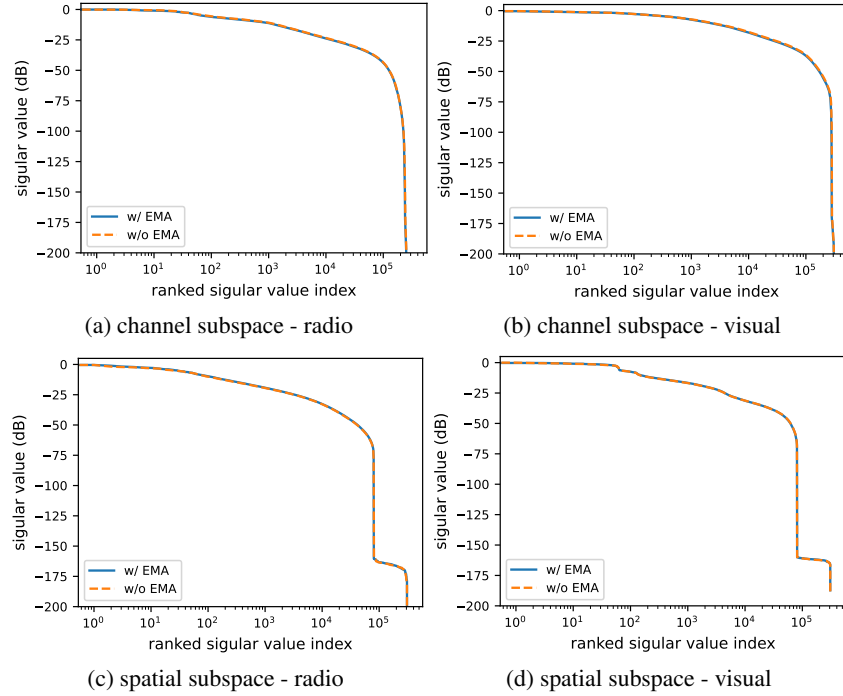


Figure 8: Radio-visual subspace analysis w/ and w/o EMA.

In Sec. 4.1, the spatial encoders $f_{\theta^r}(r), f_{\theta^v}(v) \in \mathbb{R}^{C \times h \times w}$ are introduced. Following the implementation conditions detailed in Sec. 5.2, $f_{\theta^r}(r), f_{\theta^v}(v)$ are concretely $\in \mathbb{R}^{128 \times 60 \times 80}$. In this section, we analyse their dimensionality after 100 epochs of training on the contrastive loss of Eq. 7. To do so, we evaluate these embedding tensors for the validation set. For each channel $c \in \{1, \dots, 128\}$ and spatial bin $n \in \{1, \dots, 60\} \times \{1, \dots, 80\}$, we compute the centred covariance matrices $\text{Cov}_c \in \mathbb{R}^{128 \times 128}$, $\text{Cov}_n \in \mathbb{R}^{4800 \times 4800}$ according to

$$\text{Cov}_x = \frac{1}{N} \sum_{k=0}^{N-1} (\mathbf{z}_k^x - \bar{\mathbf{z}}^x)(\mathbf{z}_k^x - \bar{\mathbf{z}}^x)^T \quad (9)$$

where \mathbf{z}_k^x is the embedding vector of a channel or spatial bin¹ $x \in [c, n]$, N is the number of validation samples, and $\bar{\mathbf{z}}^x$ is the respective average. To measure subspaces dimensionality, we compute the singular value decomposition on the covariance matrix $\text{Cov}_x = U\Sigma V^T$, $\Sigma = \text{diag}(\sigma^k)$, following general practice in SSL theory [39, 60]. We use these subspace measurements to quantify changes in the learnt contrastive representation as a result of architectural tweaks such as EMA.

¹i.e., unfolding the original 2-D spatial bins into a vector of $wh = 4800$ length

We concatenate the singular values of all channels and all spatial bins and sort them in descending order. Fig. 8 depicts on a logarithmic scale these aggregated singular values. We can readily see that EMA has little effect on the dimensionality of the learnt representation across channels and spatial bins, for both radio and vision branches. We, therefore, opt to exclude it from our experiments for efficiency.

D Radio-visual analytic relationship

In radio imaging, there are two main phenomena that govern our ability to resolve objects in space. First, range resolution Δr is determined by bandwidth B and obeys $\Delta r = c/2B$, where c is the speed of light. In typical millimetre-wave frequencies for 6G, $B \approx 1GHz$ which gives ~ 0.3 metre resolution. Second, the angular resolution $\Delta\phi$ is considerably worse and is generally related to our ability to pack antennae in a reasonable form factor. That is, the imaging performance disparity between vision and radio is largely a function of disparities in angular resolution. To see this, let $I(x, y)$ be an image of a sensing scene, where x and y are its horizontal and vertical dimensions, respectively. Let w be the so-called beamwidth of an RF horn antenna. Then the antenna response $h(x, y) = e^{-(x^2+y^2)/(2w^2)}$ is a “distortion” function associated with RF’s resolution-limited imaging of a given scene. Specifically, $h(x, y)$ will act as a blurring function that convolves with the original image according to

$$I'(x, y) = I(x, y) * h(x, y) \quad (10)$$

where I' is the degraded image and $*$ is the convolution operator.

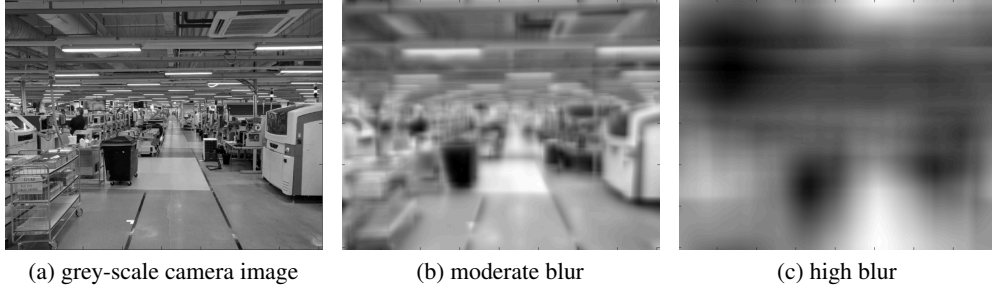


Figure 9: Radio-visual relationship. A grey-scale camera image undergoes significant blurring to simulate the effect of RF’s limited angular resolution when using radio to image the environment.

Fig. 9 contrasts normal camera imaging against RF’s resolution-limited imaging. Left-most Fig. 9a shows a grey-scale image of a factory. Assuming 1 degree angular resolution ($\Delta\phi = 1^\circ$), Fig. 9b in the middle illustrates the blurring effect of Eq. 10 on the camera image. Under higher angular resolution distortion $\Delta\phi = 10^\circ$, the right-most Fig. 9c shows significant blurring as a result of a coarser beamwidth w acting on I .

E Datasheet

We document in Tab. 6 various aspects of our radio-visual dataset according to the specifications stipulated in [61].

Table 6: Dataset datasheet

| Motivation | |
|---|--|
| For what purpose was the dataset created? | To facilitate radio-visual SSL research for 6G sensing |
| Who created the dataset and on behalf of which entity? | Bell Labs Core Research (BLCR) on behalf of Nokia |
| Who funded the creation of the dataset? | Nokia |
| Composition | |
| What do the instances that comprise the dataset represent? | heatmap-image pairs sampled from 3 scenarios |
| How many instances are there in total? | 30,000 labelled for parking lot 10,000 labeled for suburban and 10,000 labeled for canyon |
| Does the dataset contain all possible instances or is it a sample of instances from a larger set? | All |
| What data does each instance consist of? | Radio heatmaps are range-azimuth description of the environment and RGB images are their visual pairs |
| Is there a label or target associated with each instance? | For labelled set, object groundtruth coordinates for radio and scenario label. For the larger unlabelled set, no labels. |

| Cont. Tab. 6 | |
|--|---|
| Is any information missing from individual instances? | No |
| Are relationships between individual instances made explicit? | Only correspondence between a radio-visual pair |
| Are there recommended data splits? | For labelled set, 80:20 train-test split for downstream regression |
| Are there any errors, sources of noise, or redundancies in the dataset? | Not at the data instance level; It is a synthetic dataset. At the radio signal level, high-fidelity propagation modelling captures non-trivial sources of noise such as clutter and fading. |
| Is the dataset self-contained, or does it link to or otherwise rely on external resources? | Self-contained |
| Does the dataset contain data that might be considered confidential? | No |
| Does the dataset contain data that, if viewed directly, might be offensive, insulting, threatening, or might otherwise cause anxiety? | No |
| Does the dataset identify any subpopulations? | No |
| Is it possible to identify individuals, either directly or indirectly from the dataset? | No |
| Does the dataset contain data that might be considered sensitive in any way? | No |
| Collection Process | |
| How was the data associated with each instance acquired? | Synthesised using CAD tools |
| What mechanisms or procedures were used to collect the data? | Ray-tracing for radio, rendering for vision |
| If the dataset is a sample from a larger set, what was the sampling strategy? | N/A |
| Who was involved in the data collection process and how were they compensated? | Nokia employees under full-time employment |
| Over what timeframe was the data collected? | Data generation took several months of in-house development effort |
| Were any ethical review processes conducted? | N/A |
| Did you collect the data from the individuals in question directly, or obtain it via third parties or other sources? | N/A |
| Were the individuals in question notified about the data collection? | N/A |
| Did the individuals in question consent to the collection and use of their data? | N/A |
| If consent was obtained, were the consenting individuals provided with a mechanism to revoke their consent in the future or for certain uses? | N/A |
| Has an analysis of the potential impact of the dataset and its use on data subjects been conducted? | N/A |
| Preprocessing/cleaning/labeling | |
| Was any preprocessing/cleaning/labeling of the data done? | No |
| Was the “raw” data saved in addition to the preprocessed/cleaned/labeled data? | N/A |
| Is the software that was used to preprocess/clean/label the data available? | N/A |
| Uses | |
| Has the dataset been used for any tasks already? | Only radio-visual SSL research disclosed in this paper |
| Is there a repository that links to any or all papers or systems that use the dataset? | N/A |
| What (other) tasks could the dataset be used for? | This is a 1st radio-visual SSL work, and future research would build on our ideas and/or come up with alternative approaches, e.g., non-contrastive SSL |
| Is there anything about the composition of the dataset or the way it was collected and preprocessed/cleaned/labeled that might impact future uses? | No |
| Are there tasks for which the dataset should not be used? | N/A |
| Distribution | |
| Will the dataset be distributed to third parties outside of the entity on behalf of which the dataset was created? | Yes |
| How will the dataset will be distributed? | Hosted on a public website |
| When will the dataset be distributed? | 2023 |
| Will the dataset be distributed under a copyright or other intellectual property (IP) license, and/or under applicable terms of use (ToU)? | Yes |
| Have any third parties imposed IP-based or other restrictions on the data associated with the instances? | No |
| Do any export controls or other regulatory restrictions apply to the dataset or to individual instances? | No |
| Maintenance | |
| Who will be supporting/hosting/maintaining the dataset? | Nokia Bell Labs |
| How can the owner/curator/manager of the dataset be contacted? | Email |
| Is there an erratum? | No |
| Will the dataset be updated? | Yes |
| If the dataset relates to people, are there applicable limits on the retention of the data associated with the instances? | N/A |
| Will older versions of the dataset continue to be supported/hosted/maintained? | Yes |

| | |
|--|----|
| Cont. Tab. 6 | |
| If others want to extend/augment/build on/contribute to the dataset, is there a mechanism for them to do so? | No |
| End Tab. 6 | |